RMetS

Royal Meteorological Society

From accelerated warming to warming hiatus in China

Yongkun Xie, Jianping Huang* and Yuzhi Liu

Key Laboratory for Semi-Arid Climate Change of the Ministry of Education, College of Atmospheric Sciences, Lanzhou University, China

ABSTRACT: As the recent global warming hiatus has attracted worldwide attention, we examined the robustness of the warming hiatus in China and the related dynamical mechanisms in this study. Based on the results confirmed by the multiple data and trend analysis methods, we found that the annual mean temperature in China had a cooling trend during the recent global warming hiatus period, which suggested a robust warming hiatus in China. The warming hiatus in China was dominated by the cooling trend in the cold season, which was mainly induced by the more frequent and enhanced extreme-cold events. By examining the variability of the temperature over different time scales, we found the recent warming hiatus was mainly associated with a downward change of decadal variability, which counteracted the background warming trend. Decadal variability was also much greater in the cold season than in the warm season, and also contributed the most to the previous accelerated warming. We found that the previous accelerated warming and the recent warming hiatus, and the decadal variability of temperature in China were connected to changes in atmospheric circulation. There were opposite circulation changes during these two periods. The westerly winds from the low to the high troposphere over the north of China all enhanced during the previous accelerated warming period, while it weakened during the recent hiatus. The enhanced westerly winds suppressed the invasion of cold air from the Arctic and vice versa. Less frequent atmospheric blocking during the accelerated warming period and more frequent blocking during the recent warming hiatus confirmed this hypothesis. Furthermore, variation in the Siberian High and East Asian winter monsoon season supports the given conclusions.

KEY WORDS   warming hiatus; accelerated warming; cold weather events; decadal variability; atmospheric circulation

Received 7 January 2016; Revised 24 May 2016; Accepted 27 May 2016

1. Introduction

The global mean surface air temperature (SAT) has not risen significantly since 1998, a phenomenon known as the 'warming hiatus' (IPCC, 2013; Kosaka and Xie, 2013; England *et al.*, 2014; Meehl *et al.*, 2014; Trenberth *et al.*, 2014; Dai *et al.*, 2015; Guan *et al.*, 2015; Steinman *et al.*, 2015). This warming hiatus has attracted great attention worldwide and incited much debate about the theory of human-induced global warming (IPCC, 2013). So far, most studies have suggested that the warming hiatus was mainly induced by internal climate variability, e.g. strong negative-trend Pacific multidecadal variability (Steinman *et al.*, 2015), the La Niña-like cooling induced by accelerated trade winds (Kosaka and Xie, 2013; England *et al.*, 2014), and a negative phase of the Pacific Decadal Oscillation (PDO) and the Interdecadal Pacific Oscillation (Meehl *et al.*, 2014; Trenberth *et al.*, 2014; Dai *et al.*, 2015), and the negative phase of North Atlantic Oscillation (Huang *et al.*, 1998, 2006; Higuchi *et al.*, 1999; Li *et al.*, 2013; Guan *et al.*, 2015). From an energy balance perspective, the hiatus was caused by more heat being transported to deeper layers of the Atlantic Ocean and the southern oceans (Chen and Tung, 2014). These studies

indicate that the warming hiatus was mainly a result of internally generated variability, and that the warming induced by the external forcing, such as the increase in greenhouse gases, never stopped (IPCC, 2013; England *et al.*, 2015; Roberts *et al.*, 2015). Furthermore, the global mean temperature in 2015 jumped to a very high level, which made 2015 the warmest year in the period of instrumental data (indicated by the updated observational data sets: https://www.ncdc.noaa.gov/sotc/global/201513; http://www.metoffice.gov.uk/news/releases/archive/2016/2015-global-temperature; and http://www.giss.nasa.gov/research/news/20160120/). This also indicated the human-induced global warming never stopped. In addition, the external forcing, such as the reduction in the emissions of ozone-depleting substances, and a reduction in methane emissions, also were suggested to contribute to the recent warming hiatus (Estrada *et al.*, 2013). Some studies doubted or claimed the 'hiatus', which suggested the global warming did not pause, and the 'hiatus' was unsupported by observations (e.g. Karl *et al.*, 2015; Lewandowsky *et al.*, 2015). Meanwhile, some recent studies also contradicted these claims (e.g. Fyfe *et al.*, 2016). Thus, there are debates on the global warming 'hiatus'. However, for regional scales, such as the Northern Hemisphere, Eurasian continents, and China, the warming hiatus were more apparent (Duan and Xiao, 2015; Guan *et al.*, 2015; Li *et al.*, 2015).

Some studies have suggested that China also experienced the recent warming hiatus (Duan and Xiao, 2015; Li

* Correspondence to: J. Huang, Key Laboratory for Semi-Arid Climate Change of the Ministry of Education, College of Atmospheric Sciences, Lanzhou University, 222 Tianshui Road, Lanzhou 730000, China. E-mail: hjp@lzu.edu.cn

et al., 2015). As suggested by Li *et al.* (2015), the decrease of maximum temperature has contributed most to the decreases in overall mean temperature and in diurnal temperature range during the warming hiatus period. However, the Tibetan Plateau still showed the accelerated warming due to the cloud-radiation feedback (Duan and Xiao, 2015). In the Northern Hemisphere, the recent hiatus was reversed from the previous accelerated warming period, an effect that was probably related to circulation changes (Huang *et al.*, 2012; Wallace *et al.*, 2012; He *et al.*, 2014; Guan *et al.*, 2015; Huang *et al.*, 2016a). Besides, Arctic warming and sea ice decline were also suggested as influencing factors for the recent cold winters in Eurasia and North America (Cohen *et al.*, 2014; Mori *et al.*, 2014; Screen and Simmonds, 2014; Xie *et al.*, 2015).

However, some important aspects of the hiatus in China are still unclear, such as whether the hiatus in China was associated with an increase in extreme-cold weather events and by the internal climate variability. Therefore, we examined the seasonal features and robustness of the hiatus in China. We studied how daily temperatures changed during the hiatus, and the contribution made by the extreme-cold events to the hiatus. We also examined the temperature variability in China over different time scales. In addition, we explored the dynamical mechanisms about how the temperature in China changed from the previous accelerated warming to recent hiatus.

This article is arranged as follows. The details of the data sets and the methodologies used are given in Section 2. In Section 3, we discuss the seasonal and spatial features of temperature change in China. The connection between the extreme-cold events and the hiatus are presented in Section 4. Section 5 discusses the variability of the temperature changes in China over different time scales. Section 6 examines the dynamical mechanisms of the recent warming hiatus and the previous accelerated warming in China. Conclusions and discussions are presented in Section 7.

2. Data and methods

2.1. Temperature

We used monthly mean SAT data from the Climatic Research Unit (CRU) Time Series data set (version 3.23), which was provided by the University of East Anglia (Harris *et al.*, 2014). The data covered the period from 1901 to 2014 and had a resolution of $0.5° \times 0.5°$ (Harris *et al.*, 2014). The monthly and daily mean SAT data from the regular surface meteorological observations were provided by the China Meteorological Administration (CMA), and covered the period from 1951 to present. The monthly CMA SAT data had 756 observation sites. The daily CMA SAT data came from version 3.0, and had 824 observation sites. In addition, all of the sites with missing values during the studied period were removed.

2.2. Circulation data

The wind speed and geopotential height (GPH) data were taken from the National Centers for Environmental

Prediction-Department of Energy (NCEP-DOE) Reanalysis II (Kanamitsu *et al.*, 2002), and European Centre for Medium-Range weather Forecasts reanalysis (ERA)-interim (Dee *et al.*, 2011) data sets. The two data sets have a resolution of $2.5° \times 2.5°$, and include the period from 1979 to present. However, the ERA-interim data set has many different resolution choices. The sector and local blocking frequencies were calculated using daily 500-hPa GPH data same as the study conducted by D'Andrea *et al.* (1998). The sea level pressure data were taken from ERA-20C (Hersbach *et al.*, 2015) and ERA-interim (Dee *et al.*, 2011) data sets. The ERA-20C data had a resolution of $2.5° \times 2.5°$, and was for the period 1900–2010. The ERA-20C and ERA-interim data sets were merged into a longer sea level pressure data from 1900 to present, and the data for 1979–2010 period was their average. The Siberian High intensity index was calculated using monthly mean sea level pressure data as described by Gong *et al.* (2001), which was a regionally averaged sea level pressure over regions (40°–60°N, 70°–120°E). The East Asian winter monsoon (EAWM) intensity index was also calculated using monthly mean sea level pressure data as described by Wang and Chen (2014), which takes into account both the east–west and the north–south pressure gradients.

2.3. Cold weather events

Besides the monthly mean state of temperature, we also examined daily extreme weather events. To quantify the degree of the extremeness, we divided the cold events into three levels. First, the daily SAT anomalies relative to the corresponding monthly mean SAT were calculated using CMA daily SAT data. Second, the standard deviations of the daily SAT across each month were calculated. Finally, the days with negative SAT anomalies, and with absolute values >1.5, between 0.5 and 1.5, and <0.5 times the standard deviations for the corresponding month were defined as the coldest, extreme-cold, and moderate-cold events. The number of days, the mean SAT anomalies, and the sum of the SAT anomalies for the days that were identified as including in the three different levels of cold events for every month were calculated separately. Finally, these three variables for the cold season (November to the following March) were calculated for each year.

2.4. Ensemble empirical mode decomposition

We used the ensemble empirical mode decomposition (EEMD) method in our study. EEMD is an adaptive one-dimensional data analysis method, which is temporally local and therefore can reflect the nonlinear and non-stationary nature of climate data. Climate variability can be split into different oscillatory components with intrinsic timescales, including interannual, decadal, and multidecadal extents. The steps of the EEMD method that we followed were taken from Ji *et al.* (2014). In the EEMD calculation as outlined by Ji *et al.* (2014), the noise added to data had an amplitude that was 0.2 times the standard deviation of the raw data, and the ensemble number was
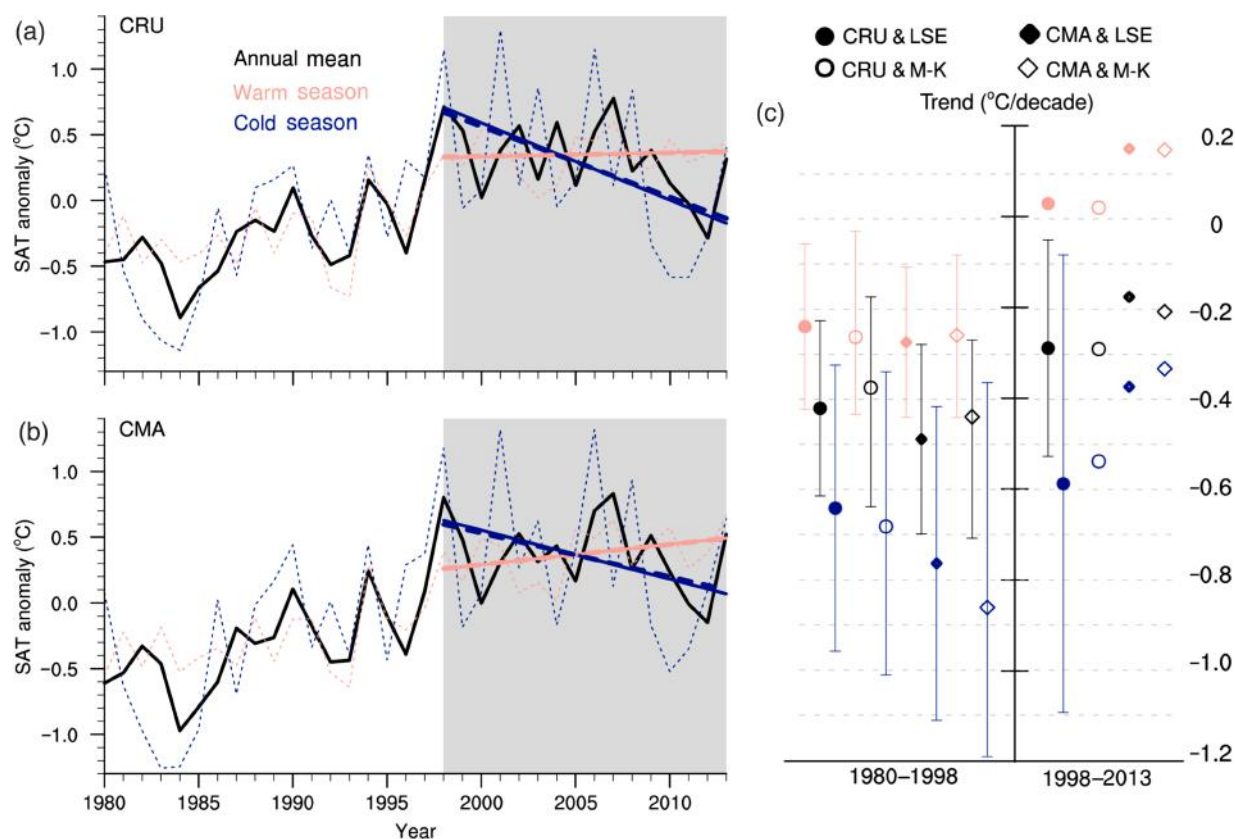
Figure 1. (a) Surface air temperature (SAT) anomaly time series averaged over China relative to the 1981–2010 reference period from the Climatic Research Unit (CRU) database. The solid lines are the linear trend lines based on the least squares estimator (LSE) for 1998–2013 for warm and cold season respectively, and the corresponding thick dashed lines are results from Mann–Kendall method (M–K). The shaded area indicates the recent warming hiatus period 1998–2013. The warm season is from May to September, and the cold season is from November to the following March. (b) Same as (a) but for results from China Meteorological Administration (CMA) dataset. (c) The SAT linear trends for 1980–1998 and 1998–2013, respectively. The solid and open circles represent the results from the LSE and M–K methods using the CRU dataset, respectively, and the corresponding rhombuses represent results from CMA dataset. The vertical bars indicate the trends are significant at 90% confidence level, and the ranges of vertical bars represent the corresponding confidence intervals at 90% confidence level (for details about the significance test methods see Section 2.5). The trends for 1980–1998 are all positive, but have been multiplied by −1 to simplify the figure. [Colour figure can be viewed at wileyonlinelibrary.com].

400. The number of intrinsic mode functions was six. A MATLAB EMD/EEMD package with the above stoppage criteria and end treatments is available for download at http://rcada.ncu.edu.tw/research1.htm (Wang *et al.*, 2014).

2.5. Methods of the trend calculations

We used simple linear regression method that based on least squares estimator (LSE) to calculate the trend. The corresponding significance and confidence interval were estimated by using the two-tailed Student's *t*-test. Furthermore, we also used the Mann–Kendall (M–K) method (Mann, 1945; Kendall, 1948) to confirm the results from the simple LSE method. M–K method has been suggested to perform better than LSE especially for the data that are not normally distributed and include extreme values (Wang and Swail, 2001). To avoid the influences of the autocorrelation on significance test (Lee and Lund, 2004), we used the 'prewhiten' method as conducted by Wang and Swail (2001). We performed the same procedures of M–K method as described in 'Appendix A' of Wang and Swail (2001). As homogeneity of data is important for

trend analyses, we therefore compared our results with the work by Li *et al.* (2015) that used the homogenized temperature data in China (Li *et al.*, 2009; Xu *et al.*, 2013). The results showed that the spatial patterns of the temperature trends from Li *et al.* (2015) were consistent with our results.

2.6. Climate indexes

The Niño 3.4 index is the sea surface temperature (SST) averaged over (5°S–5°N, 170°–120°W), available from http://www.esrl.noaa.gov/psd/data/correlation/nina34. data. The PDO index is derived as the leading principal component of monthly SST anomalies in the North Pacific Ocean, poleward of 20°N with the monthly mean global average SST anomalies are removed, available from http://research.jisao.washington.edu/pdo/PDO.latest.

3. SAT evolution in China

Figure 1 shows the SAT evolution in China from 1980 onward taken from CRU and CMA data sets respectively.
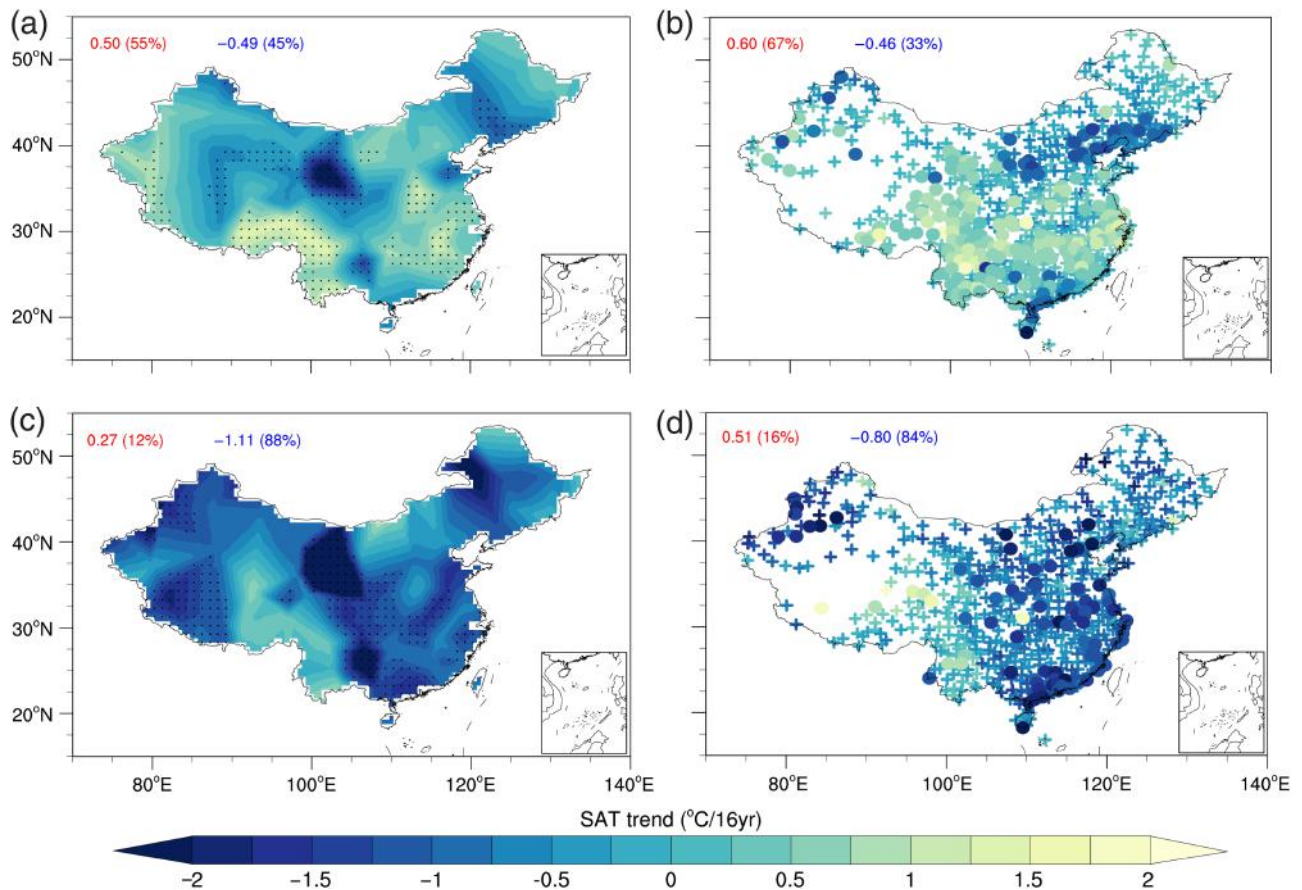
Figure 2. (a) SAT trends in China for 1998–2013 during the warm seasons from the CRU dataset. The numbers are the area weighted mean trends for the warming (positive trends) and cooling (negative trends) regions, respectively. The numbers in the brackets are the areal percentages of warming and cooling regions relative to the total area of China, respectively. The trends were calculated using the simple linear regression based on the LSE method. The black dots represent the trends are significant at 90% confidence level. (b) Same as (a) but for results from the CMA dataset. The solid circles represent the trends are significant at 90% confidence level. (c), (d) Same as (a), (b) but for the cold seasons. Note that the same figure but for using the M–K method is presented in the Supporting Information as Figure S1. [Colour figure can be viewed at wileyonlinelibrary.com].

As shown in Figure 1(a) and (b), China has been experiencing an apparent warming hiatus since 1998. However, the hiatus is more significant during cold seasons than during warm seasons (Trenberth *et al.*, 2014; Duan and Xiao, 2015; Guan *et al.*, 2015; Li *et al.*, 2015). As a result, the cold seasons have experienced an apparent cooling trend since 1998, while there have still been weak warming trends during the warm season (Figure 1(a) and (b)). Both CRU data and CMA data gave the same results. Furthermore, the SAT switched from a previously accelerated warming period to a recent warming hiatus. Figure 1(c) shows the trends of the mean SAT in China for 1980–1998 and for 1998–2013 respectively. For simplicity, the positive trends for 1980–1998 in Figure 1(c) were multiplied by −1 to change the values to negative values. As shown in Figure 1(c), the temperature in China showed significant warming trends, and the warming trends during the cold seasons were much larger than during the warm seasons for 1980–1998. For 1998–2013, the temperature for annual and cold season showed cooling trends, although which were only significant for the CRU data set and using the LSE method. However, these were enough to indicate a slowdown of the warming trends in China, and the

warming hiatus indeed existed in China (Li *et al.*, 2015). For both the accelerated warming period and the recent warming hiatus period, the SAT changes during the cold seasons made the greatest contributions to the SAT trends (Figure 1(c)). The differences between the CRU and the CMA data in Figure 1 were mainly induced by the varied resolutions of the CMA data over different regions.

Figure 2 shows the spatial patterns of the SAT trends during the hiatus period for the warm and cold seasons. As shown in Figure 2(a) and (b), many regions still experienced the warming trends during the warm seasons. The warming regions occupied 55 and 67% of the total area in the CRU and CMA data sets, respectively, and the mean warming trends were larger than the cooling trends for both data sets (Figure 2(a) and (b)). The regions with the greatest warming rates during the warm seasons were northeastern China and the Tibetan Plateau. During the cold season, most of the regions experienced cooling trends, and the cooling regions occupied 88 and 84% of the total area in the CRU and CMA data sets, respectively (Figure 2(c) and (d)). In addition, the mean cooling trends were much larger than the warming trends during the cold seasons. Same as Duan and Xiao (2015) suggested, the
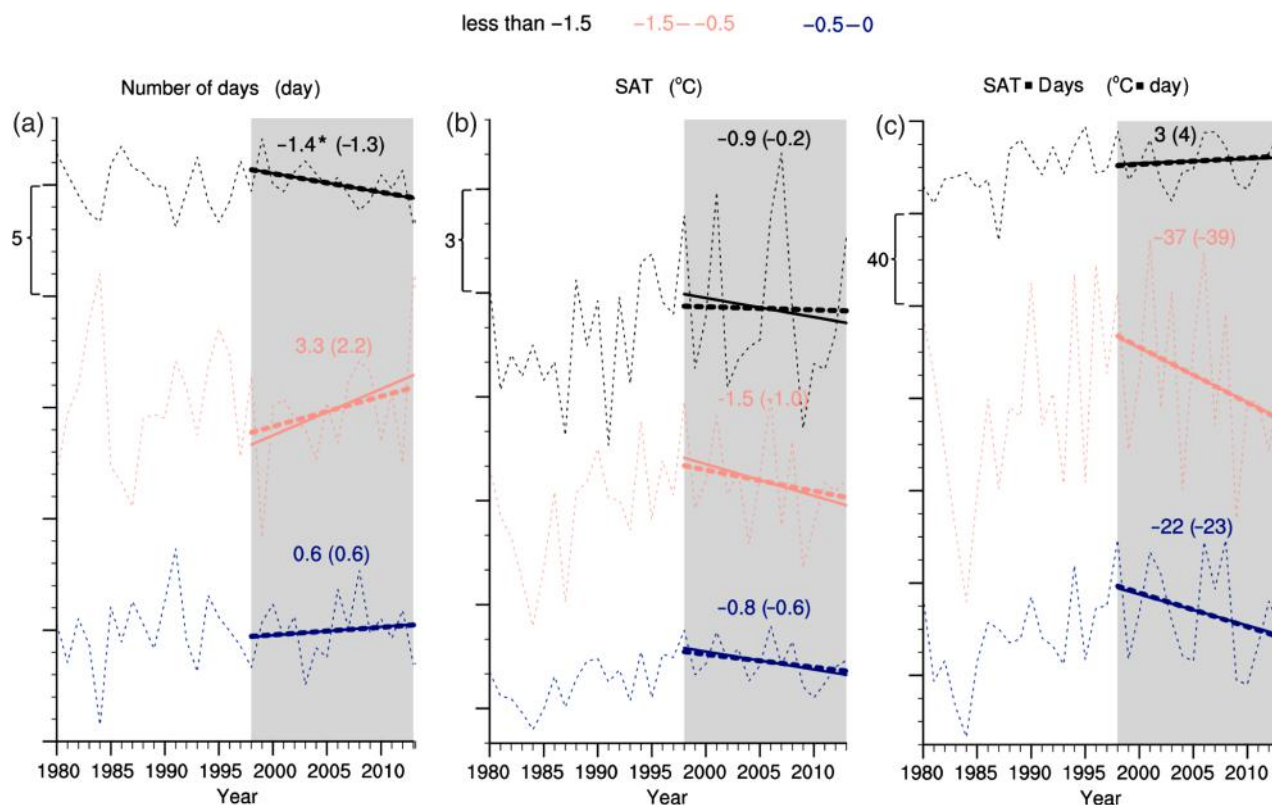
Figure 3. (a) Time series of the number of days with three levels of cold events in China during the cold seasons. The solid lines are the linear trend lines based on the LSE method for 1998–2013, while the corresponding thick dashed lines are results from M–K method. The numbers out or in the brackets represent the values of trends from LSE and M–K methods, respectively. The asterisk represents the trend is significant at 90% confidence level. The shaded area indicates the recent warming hiatus period 1998–2013. The three levels of cold events were defined based on the daily temperature. The days with negative SAT anomalies and absolute values greater than 1.5, between 0.5 and 1.5, and less than 0.5 times the standard deviations for the corresponding month were defined as coldest, extreme-cold, and moderate-cold events (for details see Section 2.3). Note that the climatology of the days for the coldest, extreme-cold, and moderate-cold events for 1981–2010 were 10, 39, and 27, respectively. (b) Same as (a) but for the mean SAT for the three kinds of cold events. (c) Same as (a) but for the sum of the SAT anomalies for the three kinds of cold weather events. [Colour figure can be viewed at wileyonlinelibrary.com].

Tibetan Plateau showed obvious warming trends for both warm and cold seasons. The same conclusions were indicated by Figure S1 in the Supporting Information, which used the M–K method to calculate the trends.

4. The contribution of cold weather events

Figure 3 shows the evolution of the number of days, mean SAT anomalies, and the sum of the SAT anomalies for the three levels of cold weather events during the cold seasons, as well as details about the methods discussed in Section 2.3. Among the three levels of cold weather events, the extreme-cold event is more representative, because the coldest event is too extreme and rare, and the moderate-cold event is weak as a kind of extreme events. The climatology of the days for the coldest, extreme-cold, and moderate-cold events during 1981–2010 were 10, 39, and 27, respectively. As shown in Figure 3(a), the number of coldest days decreased slightly, and the number of the moderate-cold days increased slightly. However, the number of extreme-cold days increased apparently. Meanwhile, the mean SAT decreased for all three levels of cold events, and the mean SAT of extreme-cold

events decreased the most (Figure 3(b)). Therefore, the increased numbers of extreme-cold events and its largest cooling trends of mean SAT values together made the greatest contributions to the recent warming hiatus in China (Figure 3(c)). The moderate-cold events also contributed to the recent cooling during the cold seasons in China (Figure 3(c)). However, because the number of coldest days decreased, the coldest events contributed little to the hiatus (Figure 3(c)).

Figure 4 shows the spatial patterns of the contributions of the three levels of cold events to the SAT trends during the recent warming hiatus. As shown in Figure 4(a), there was an almost equal amount of warming contribution and cooling contribution from the coldest events, and the magnitude of the contributions was also relatively weaker than the other two kinds of cold events. Although the mean SAT of the coldest events decreased in many regions, the number of days decreased at the same time, so many regions showed warming contributions (Figure 5(a) and (b)). Both extreme- and moderate-cold events showed a cooling contribution in most regions. However, the extreme-cold events had larger magnitudes than the moderate-cold events in many regions than moderate-cold
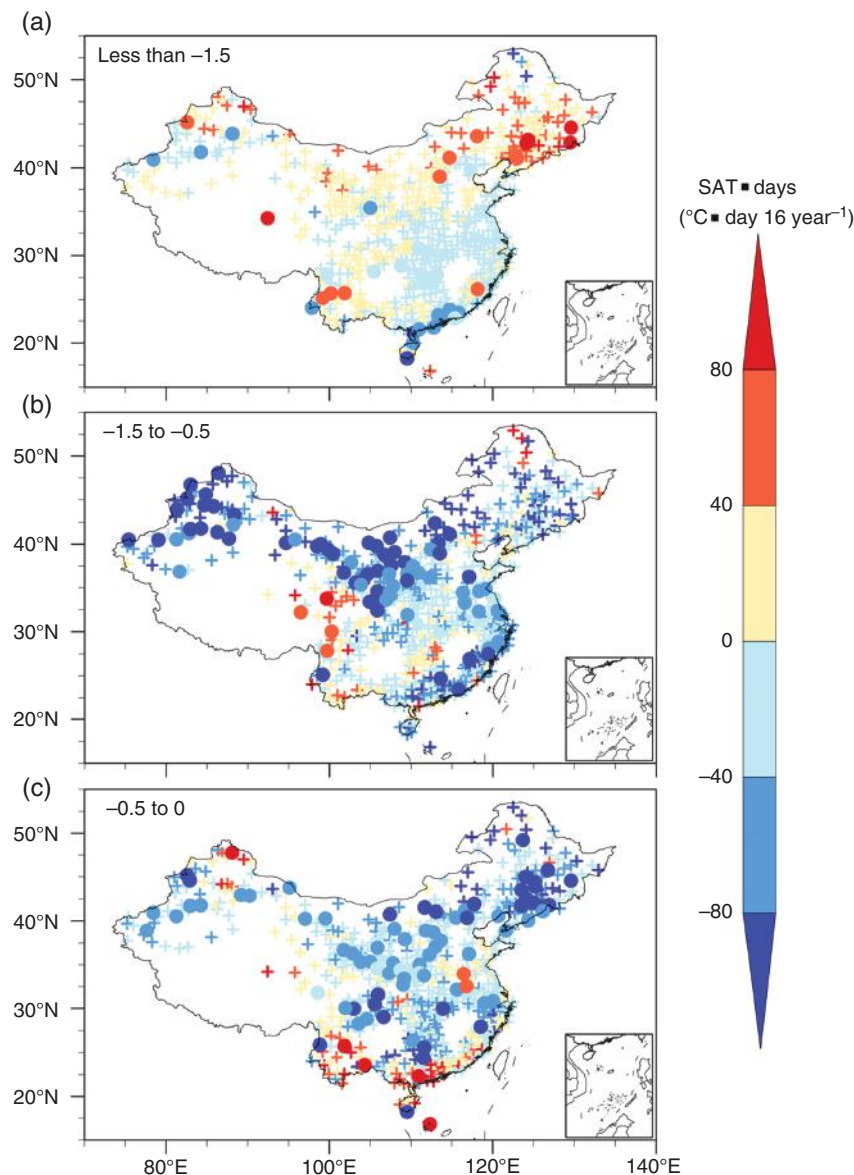
Figure 4. (a) The linear trends of the sum of the SAT anomalies for the coldest events from 1998 to 2013 in China during the cold seasons. The trends were calculated using the simple linear regression based on the LSE method. The solid circles represent the trends are significant at 90% confidence level. (b) and (c) are same as (a) but for extreme-cold and moderate-cold events, respectively. Note that the same figure but for using the M–K method is presented in the Supporting Information as Figure S2. [Colour figure can be viewed at wileyonlinelibrary.com].

events, especially in northern China (Figure 4(b) and (c)). The mean SAT in most regions showed cooling trends for both extreme- and moderate-cold events (Figure 5(d) and (f)). However, the number of days with extreme-cold events increased apparently more than the number of days with moderate-cold events, especially for the central and southeastern regions of China (Figure 5(c) and (e)). The same conclusions were indicated by Figures S2 and S3 in the Supporting Information, which used the M–K method to calculate the trends.

5. Variability of temperatures over different time scales

To examine the evolutions of temperatures in China in depth, we decomposed the time series of SAT into different time scales using the EEMD decomposition method (for details about the EEMD method, see Section 2.4). The decomposed SAT time series were divided into three time scales including interannual variability, decadal variability, and long-term trends. The interannual variability is the sum of the first and second intrinsic mode functions from EEMD decomposition. The decadal variability is the sum of the third to fifth intrinsic mode functions. The long-term trend is the sixth intrinsic mode function. Figure 6 shows the interannual variability, decadal variability, and long-term trends of the annual mean SAT anomalies in China. As shown in Figure 6, the annual mean SAT in China showed obvious large interannual and decadal variability, as well as significant background long-term warming trends. For the recent warming hiatus period, decadal variability showed a significant cooling
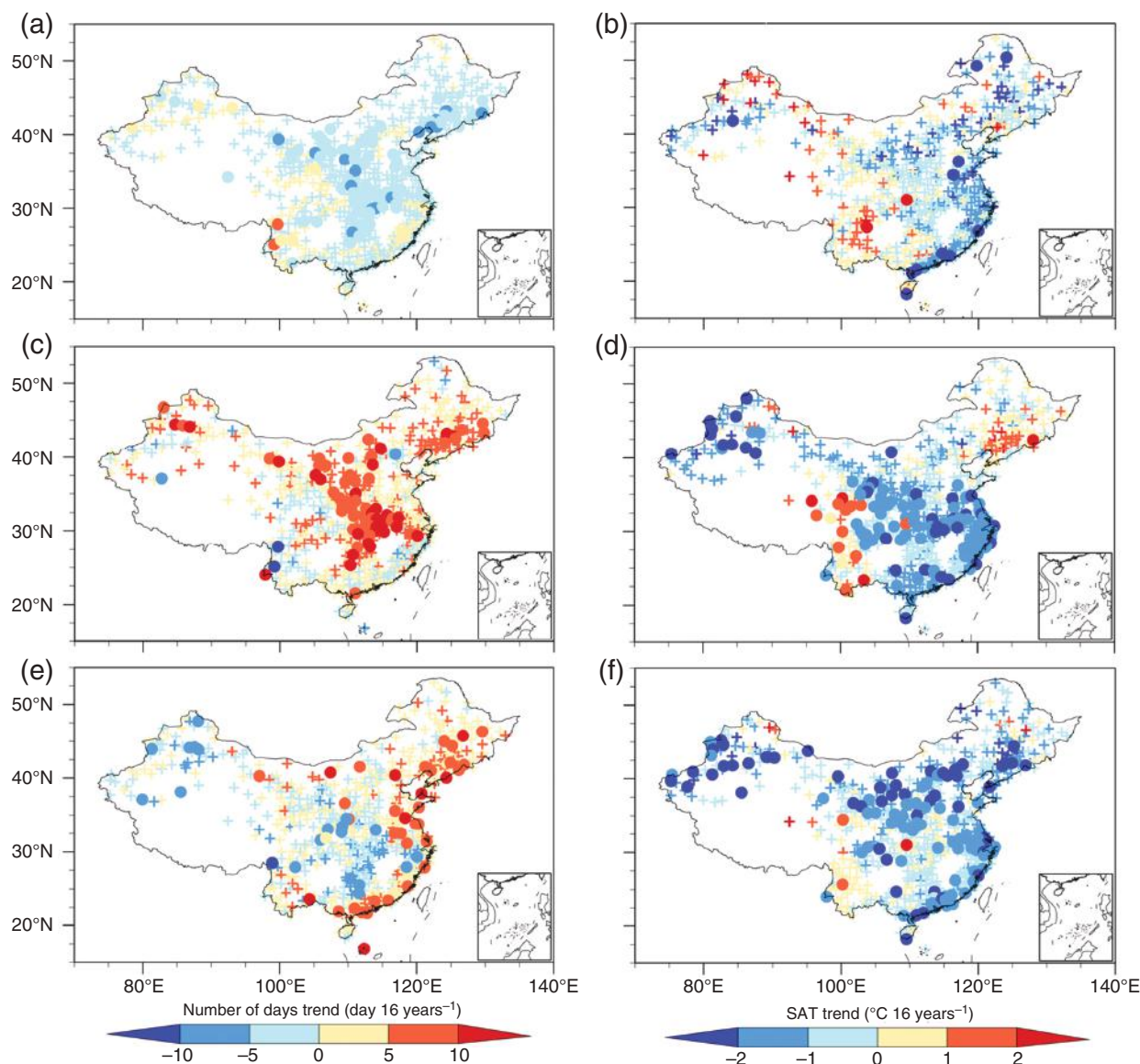
Figure 5. (a), (c), and (e) are same as Figure 4(a)–(c) but for the linear trends of the number of days. (b), (d), and (f) are same as (a), (c), and (e) but for the linear trends of the mean SAT. Note that the same figure but for using the M–K method is presented in the Supporting Information as Figure S3. [Colour figure can be viewed at wileyonlinelibrary.com].

trend, which was corresponding to the warming hiatus (Figure 6). The interannual variability has little influence on trends in decadal scale, although the interannual variability showed a weak cooling trend during the recent warming hiatus (Figure 6). As shown in Figure 6, for any decade, the magnitudes of the SAT changes in China induced by the decadal variability may be comparable with, or even larger than, the background warming trends (Trenberth, 2015).

Figure 7 shows the interannual variability, decadal variability, and long-term trends of the mean SAT in China for the warm and cold seasons, respectively. As shown in Figure 7, the amplitude of the interannual variability in the cold seasons was greater than in the warm seasons, which indicates the greater influence of atmospheric circulation variability on SAT during cold seasons (Wallace *et al.*, 2012). Regarding decadal variability, the cold season

showed quite a large cooling trend during the recent warming hiatus, while the warm season changed little (Figure 7). The long-term warming trend for the cold seasons was also greater than for the warm seasons. Additionally, the decadal variability for the cold seasons also showed a greater warming trend than did the warm seasons during the previous accelerated warming period. Therefore, the temperature in cold seasons experienced larger decadal changes during both the previous accelerated warming and the recent warming hiatus than did the warm seasons (Figure 7).

The hiatus was mainly the result of the downward decadal variability counteracted the background warming trend, while the accelerated warming was a result of the upward decadal variability in combination with the background warming trend (Figures 6 and 7). Figure 8 shows the spatial patterns of the SAT trends for 1980–1998 in
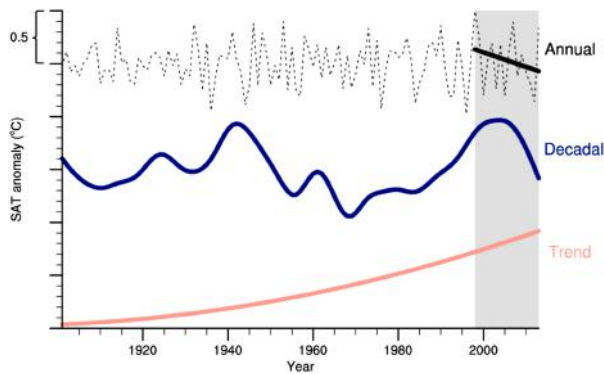
Figure 6. Decomposition of the annual mean SAT anomaly time series averaged over China into different time scales using the ensemble empirical mode decomposition (EEMD) method. The dashed curve represents the interannual variability series, which is the sum of the first two intrinsic mode functions from the EEMD (for details see Section 2.4). The solid line is the trend line based on the LSE method for 1998–2013. The two solid curves represent the decadal variability and the background long-term warming trend, which were the sum of the third to fifth, and the sixth intrinsic mode functions from the EEMD, respectively. [Colour figure can be viewed at wileyonlinelibrary.com].
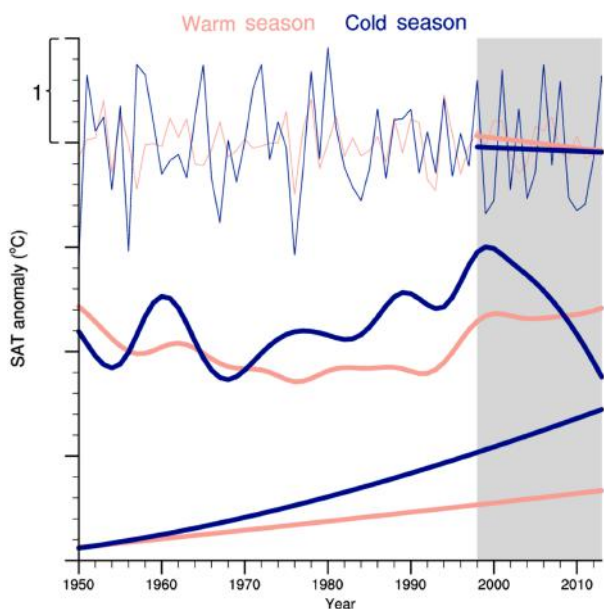

Figure 7. Same as Figure 6 but for warm and cold seasons, respectively. [Colour figure can be viewed at wileyonlinelibrary.com].

both warm and cold seasons. As shown in Figure 8, the warming trends during the cold seasons were much greater than during the warm seasons for the accelerated warming period. For the warm seasons, the warming regions accounted for 55 and 85% of the total area for the CRU and CMA data, respectively, and the mean warming trends were slightly greater than the cooling trends. However, almost all of the regions in China experienced warming trends during the cold seasons except for 0.3 and 2% cooling regions for CRU and CMA data, respectively. The same conclusions were indicated by Figure S4 in the Supporting Information, which used the M−K method to calculate the trends. In addition, as the background trends

of SAT were positive (Figures 6 and 7), the SAT trends were almost uniformly warming during the previous accelerated warming period when the positive trends induced by upward decadal variability combined with the background positive trends (Figure 8). However, the SAT trends during the warming hiatus period were not uniformly negative (Figure 2), because the negative trends induced by the downward decadal variability were not larger than the background positive trends in some regions.

6. Dynamics from accelerated warming to warming hiatus

The previous accelerated warming and the recent warming hiatus in China were both primarily corresponding to the downward decadal variability of temperature during cold seasons (Figures 6 and 7). A key question, therefore, is what are the dynamic mechanisms behind the decadal variability of temperature in China. The surface solar radiation in China experienced the transition from solar dimming to a levelling-off circa 1990 (Wang and Dickinson, 2013; Wang and Yang, 2014; Folini and Wild, 2015; Lin *et al.*, 2015), which indicated that the surface solar radiation changed little during the recent warming hiatus period. We therefore focused on the influences of large-scale advection and air masses changes on the temperature changes in China. We first examined large-scale circulation changes. Figure 9 shows the evolution of 500-hPa circulations during the cold seasons for both the previous accelerated warming period and the recent warming hiatus period. The climatology of the turning period 1994–2003, and the trends for both 1980–1998 and 1998–2013 are shown in Figure 9. As shown in Figure 9(a), China was under the background of westerlies circulation, and influenced by the East Asia deep trough. For the previous accelerated warming period, a general figure is the opposite change between the high-latitude and the mid-latitude GPH. In this context, the general figure induced the stronger meridional GPH gradients and correspondingly stronger westerly winds over the North of China regions (Figure 9(b)). However, the opposite situation with weakened meridional GPH gradients and westerly winds over the North of China occurred during the recent warming hiatus (Figure 9(c)). The enhanced westerly winds over the North of China can suppress the invasion of cold air from the Arctic, and as a result, the accelerated warming occurred, and vice versa for recent warming hiatus.

Figure 10 shows the evolution of the vertical profiles of the zonal winds, averaged across the 75°−135°E regions. The climatology for 1994–2003 and the trends for both the 1980–1998 and 1998–2013 periods are shown in Figure 10. As shown in Figure 10(a), China was influenced by westerly winds from the surface to the upper troposphere, and by a strong westerly jet around 30°N in the upper troposphere. The westerly wind speed increased during the previous accelerated warming period over 40°−65°N regions, especially in the middle to upper troposphere (Figure 10(b)). However, the speed of the
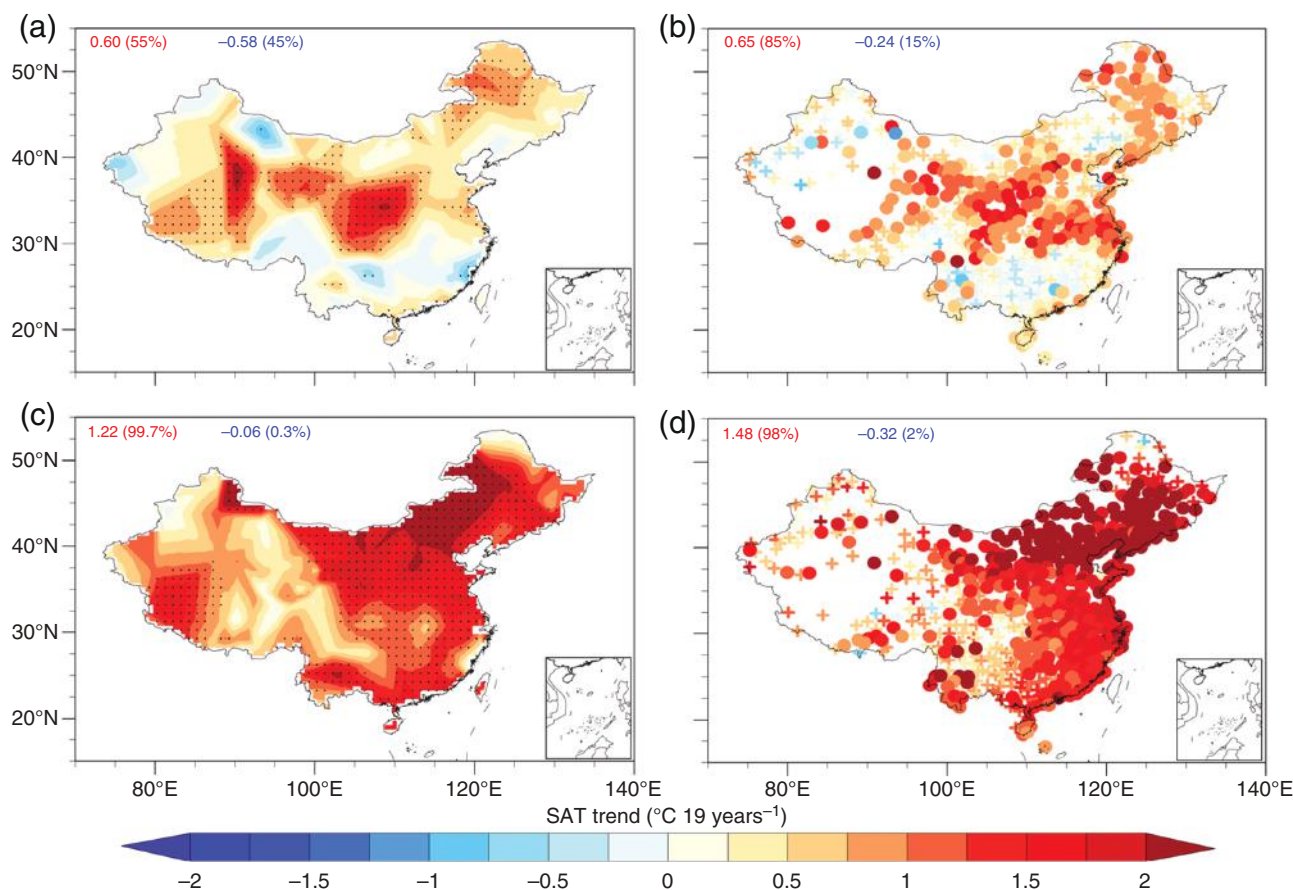
Figure 8. Same as Figure 2 but for the 1980–1998 period. Note that the same figure but for using the M–K method is presented in the Supporting Information as Figure S4. [Colour figure can be viewed at wileyonlinelibrary.com].

westerly winds decreased during the recent warming hiatus (Figure 10(c)), which is the opposite of what occurred during the previous accelerated warming period.

The stronger westerly winds over the North of China can suppress the southward cold air from high-latitudes to invade China and the formation of atmospheric blocking, and vice versa for the weaker westerly winds. So we also examined the changes in atmospheric blocking. Figure 11 shows the evolution of the blocking frequency in China. The time series for both the sector blocking frequency and the local blocking frequency were calculated using the method of D'Andrea *et al.* (1998) and are presented in Figure 11. As shown in Figure 11(a), the sector blocking frequency in China decreased during the accelerated warming period and increased during the recent warming hiatus. In turn, the SAT in China increased with the decreasing blocking but decreased with the increasing blocking. The local blocking frequency in the 70°–140°E regions also decreased for almost all of the longitudes from the beginning high frequency to a minimum frequency, and then increased during recent warming hiatus (Figure 11(b)). The increased frequency of blocking in China also explains the increase in extreme- and moderate-cold weather events during the recent warming hiatus, as shown in Figures 3–5. The opposite changes in the blocking frequency confirm the opposite circulation

changes for the previous accelerated warming period and the recent warming hiatus period.

We also examined the Siberian High and EAWM, because they influence the climate in China, especially during the cold seasons (Gong *et al.*, 2001; Wang and Chen, 2014). Figure 12 shows the time series of Siberian High and EAWM intensity indexes for the means from December to the following February. The Siberian High intensity index was defined same as the index defined by Gong *et al.* (2001), and the EAWM intensity index was defined same as the index defined by Wang and Chen (2014). As shown in Figure 12(a), the Siberian High has large interannual variability and obvious decadal variability. The Siberian High intensity showed a decreasing trend during the previous accelerated warming period and an apparent increasing trend during the recent warming hiatus (Figure 12(a)). The EAWM showed a more obvious weakened trend during the previous accelerated warming period and an enhanced trend during the recent warming hiatus (Figure 12(b)). As the Siberian High and EAWM were highly correlated, they showed similar variation. Thus, changes in both Siberian High and EAWM confirmed the connection of the accelerated warming and the warming hiatus with atmospheric circulation changes.

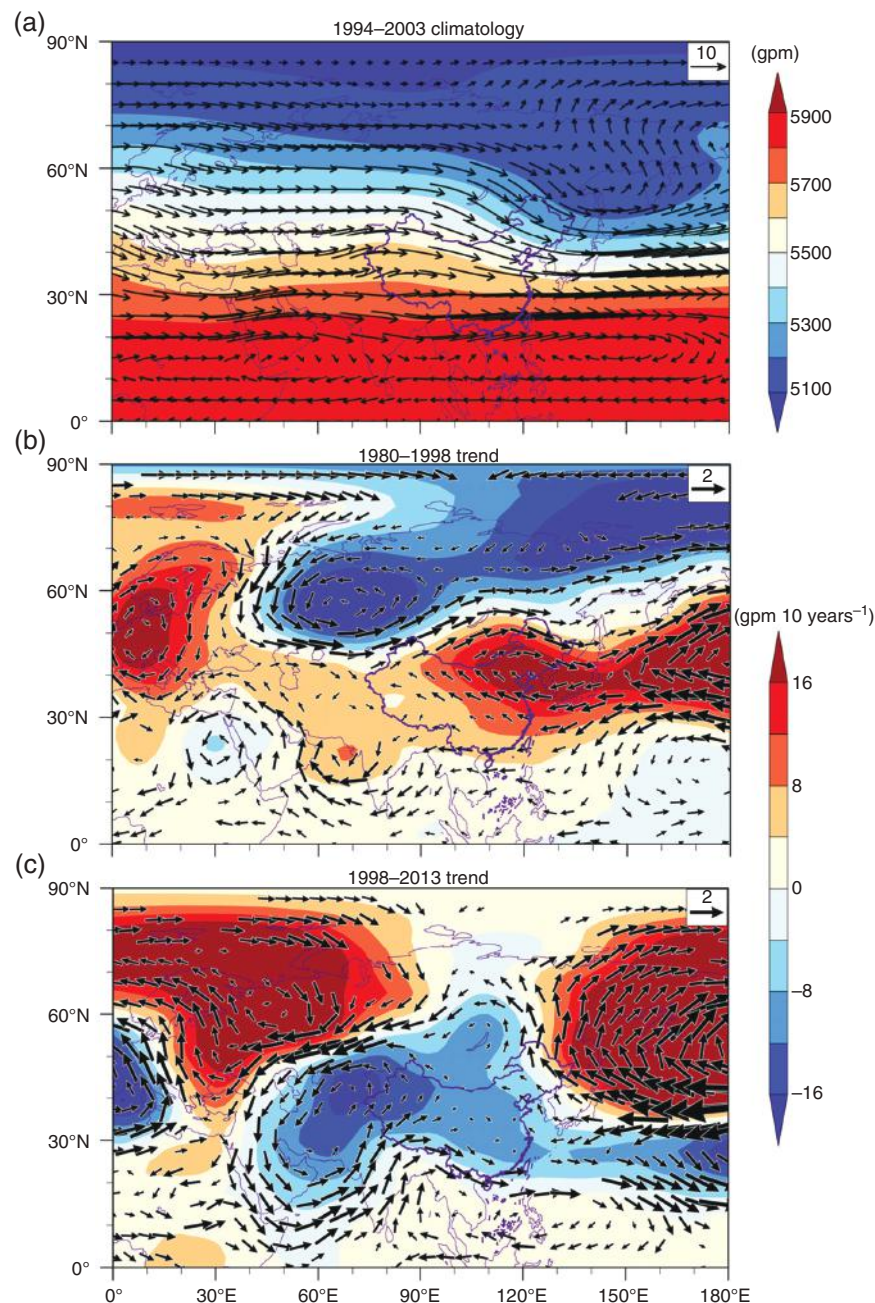Many studies suggested the important influences of the Pacific's variability on the recent warming hiatus

Figure 9. (a) Climatology of the 500-hPa circulation around China for the period 1994–2003. The filled contours represent the GPH field. The vectors represent the corresponding wind field. Note that the results are the mean of the ERA-interim and NCEP II data sets. (b) Same as (a) but for trends for 1980–1998. The trends are calculated using the simple linear regression based on the LSE method. Only the wind vectors over the regions where the meridional and zonal wind speed trends from the ERA-interim and NCEP II data sets had the same signs are presented. (c) Same as (b) but for the period 1998–2013. [Colour figure can be viewed at wileyonlinelibrary.com].

(Kosaka and Xie, 2013; England *et al.*, 2014; Meehl *et al.*, 2014; Trenberth *et al.*, 2014; Dai *et al.*, 2015). Some discussions about the Pacific's influences on the recent warming hiatus in China were also performed. As suggested by Trenberth *et al.* (2014), the PDO and El Niño/Southern Oscillation (ENSO) influence extratropical regions through the Rossby waves, as well as, the corresponding upper tropospheric teleconnection wave patterns. We therefore explored the PDO and ENSO's influences on upper tropospheric circulation. Figure 13 shows the spatial pattern of the correlation coefficients between the PDO, Niño 3.4 indexes, and the 200-hPa zonal winds, respectively. The PDO's correlation patterns with 200-hPa zonal winds were similar with that of ENSO, but the ENSO shows stronger correlations than PDO, especially a significantly correlated centre presented in China (Figure 13(b)). As a consequence, the PDO shows no significant influences on zonal winds over the regions of East Asian westerly jet represented by the green line and pentagram (Figures 13(a) and S5). The ENSO shows negative correlations significant at 99% confidence level over the regions of westerly jet around Japan, but it was also not a very
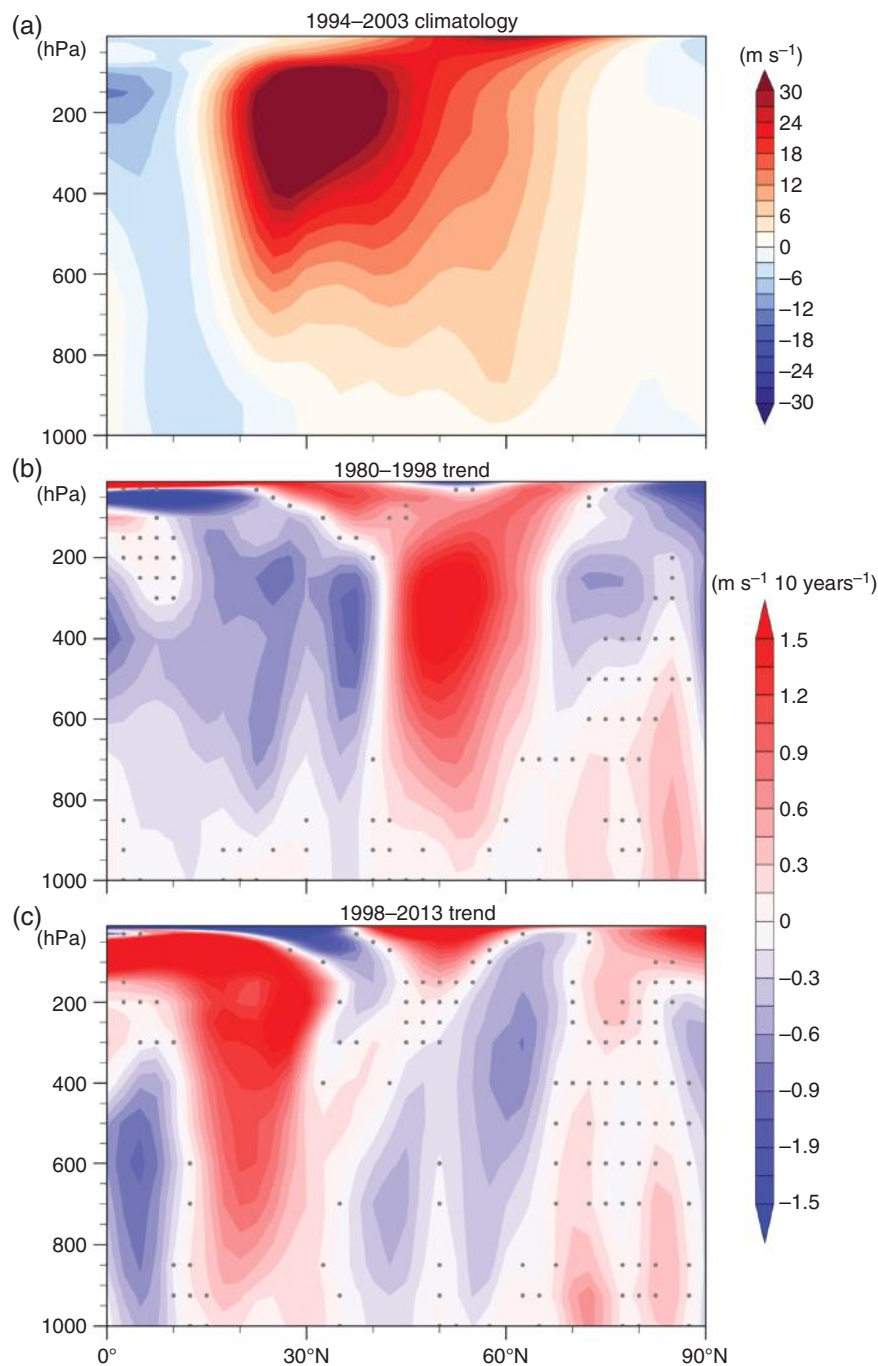
Figure 10. (a) Climatology of the zonal wind profiles, averaged over the 75°–135°E regions for the 1994–2003 period. Note that the results are the mean of the ERA-interim and NCEP II data sets. (b) Same as (a) but for trends for 1980–1998. The trends are calculated using the simple linear regression based on the LSE method. The black dots indicate the regions where the signs of the trend from the ERA-interim and NCEP II data sets did not agree. (c) Same as (b) but for the 1998–2013 period. [Colour figure can be viewed at wileyonlinelibrary.com].

strong correlation (Figure 13(b)). The PDO and ENSO's influences on westerly jet therefore were not significant during the recent warming hiatus. For both PDO and ENSO, there was an obvious wave pattern from tropical Pacific to extratropical Pacific similar with Trenberth *et al.* (2014). For ENSO, there was also another wave pattern originated from the tropical Indian Ocean across China (Figure 13(b)). Thus, a possible way of ENSO's influence on China is from tropical Pacific to the Indian Ocean, and then from the Indian Ocean to China. In addition,

both the PDO and ENSO were suggested to influence the EAWM, especially for the interdecadal variability (Zhou *et al.*, 2007; Wang *et al.*, 2008; Chen *et al.*, 2013; Ding *et al.*, 2014), which suggested the possible connections between the enhanced EAWM during the recent warming hiatus with the La Niña phase of ENSO and negative phase of PDO. However, as the PDO and ENSO's influence on China was quite complex, the more robust and clearer conclusions could be achieved only by more studies concerning the explicit dynamical mechanisms, such as
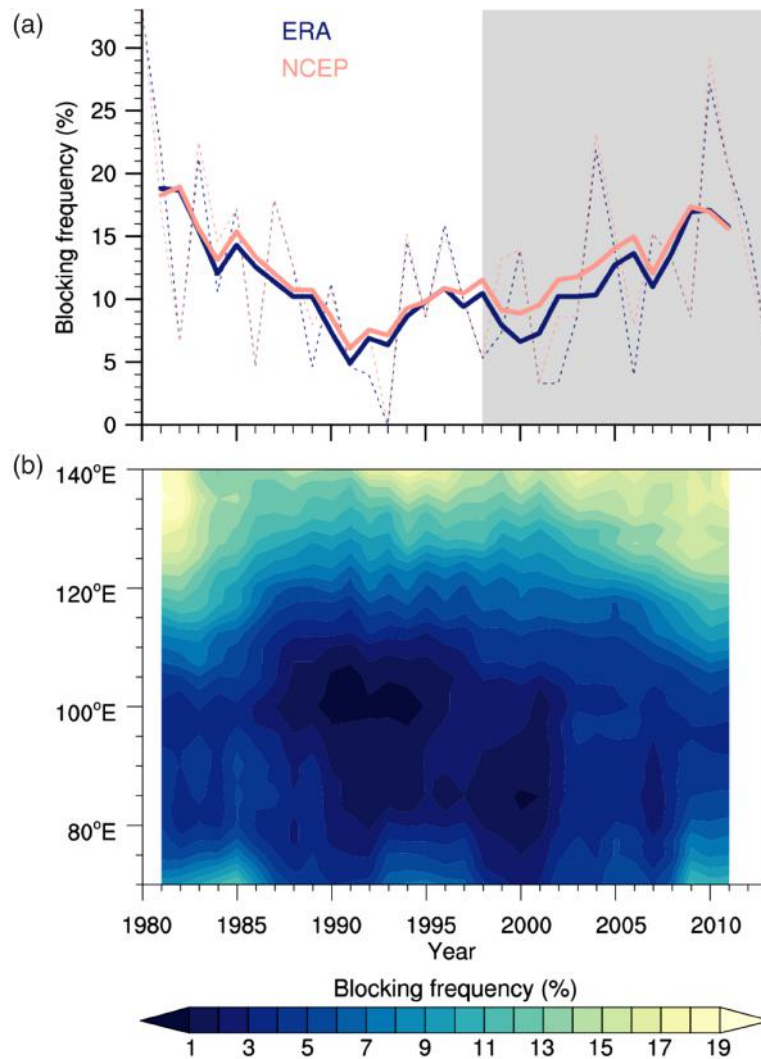
Figure 11. (a) The time series of the sector blocking frequencies for the cold seasons in 70°–140°E regions. The dashed curves represent original series from the NCEP II and ERA-interim datasets, and the solid curves represent series with 5 years of running means. (b) The local blocking frequency with 5 years of running means for the cold seasons. Note that the sector and local blocking frequencies are calculated using the method described by D'Andrea *et al.* (1998). [Colour figure can be viewed at wileyonlinelibrary.com].

the studies by using the simulations from coupled climate models.

7. Conclusions and discussions

Using the CRU grid data and CMA regular surface meteorological observations, we showed the robustness of the warming hiatus that occurred in China. This warming hiatus was mainly induced by the cooling trend during the cold seasons. Furthermore, it was an accelerated warming period before the recent warming hiatus, which also mainly occurred during the cold seasons. In addition, further analyses about the daily temperature change were performed to examine the contribution of cold weather events to mean temperature changes in China. We divided the cold events into three levels with the strength from high to low, denoted as coldest, extreme-cold, and moderate-cold events. We found that there were

more extreme- and moderate-cold events, and the former increased the most, while there were less coldest events. The mean temperatures for all three kinds of cold events decreased during the warming hiatus period, but decreased most for the extreme-cold events. Therefore, the extreme-cold events contributed the most to the recent warming hiatus, though the moderate-cold events also contributed significantly. However, the coldest events showed little contribution. The number of the extreme-cold events increased in most regions in China, especially in the central and southeastern regions during the warming hiatus period, while the number of moderate-cold events increased mainly in the northeastern regions. The mean temperature decreased in most regions for both extreme- and moderate-cold events during the warming hiatus period. Thus, the extreme- and moderate-cold events had cooling contributions in most regions in China.

We examined the variability of temperatures in China over different time scales using the EEMD method. The
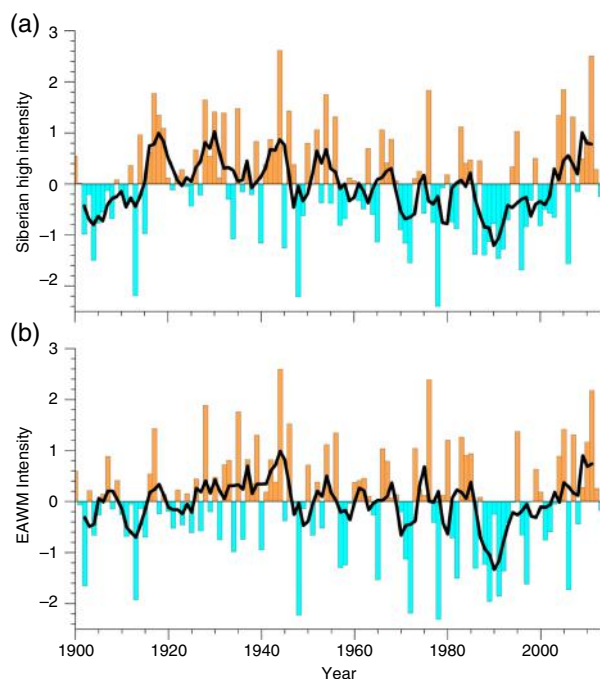
Figure 12. (a) The time series of the normalized Siberian High intensity index for the means from December to the following February calculated using the method described by Gong *et al.* (2001). The bars represent the original series, and the black curve represents the series with 5 years of running means. (b) Same as (a) but for the EAWM intensity index, as calculated by Wang and Chen (2014). [Colour figure can be viewed at wileyonlinelibrary.com].

temperatures in China showed large decadal variability and interannual variability, and the decadal variability showed large warming or cooling trends at the decadal time scale, which was comparable with the background long-term warming trend. The recent warming hiatus was mainly corresponding to the downward change of decadal variability, which counteracted the background warming trend. Decadal variability also contributed greatest to the previous accelerated warming period, which was induced by the upward decadal variability in combination with the background warming trend. The decadal variability was greater for the cold seasons than for the warm seasons. The previous accelerated warming period and the recent warming hiatus period were both mainly associated with decadal variability during the cold seasons.

To examine the dynamic mechanisms responsible for the previous accelerated warming and the recent warming hiatus, we analysed the middle troposphere atmospheric circulations and the vertical profiles of zonal winds, atmospheric blocking, and Siberian High and EAWM. There were opposite changes in the atmospheric circulations for the previous accelerated warming and the recent warming hiatus periods. The westerly winds over the North of China at 500-hPa were significantly enhanced during the previous accelerated warming period, while they were weakened during the recent warming hiatus. The vertical profile of the zonal winds also showed enhanced trends over the North of China from low to high troposphere during the accelerated warming period, while they

were weakened during the recent warming hiatus. These enhanced westerly winds can suppress the invasion of cold air from the Arctic, and vice versa with respect to the weakened westerly winds. Indeed atmospheric blocking in China regions decreased during the previous accelerated warming period, but became more frequent during the recent warming hiatus period. The variation of atmospheric blocking also explained the increased frequency of the extreme- and moderate-cold events in China during the warming hiatus period. In addition, the variation of the Siberian High and EAWM also showed weakened trends during the previous accelerated warming period, but obviously enhanced trends during the recent warming hiatus period.

We showed that both the previous accelerated warming period and the recent warming hiatus in China were mainly associated with the decadal variability, which is related to atmospheric circulation changes. However, as most studies on the subject suggest, the recent global warming hiatus was mainly induced by internal climate variability (Chen and Tung, 2014; Meehl *et al.*, 2014; Dai *et al.*, 2015; Guan *et al.*, 2015; Steinman *et al.*, 2015), especially the decadal variability of the Pacific ocean (England *et al.*, 2014; Dai *et al.*, 2015; Steinman *et al.*, 2015). Therefore, the atmospheric circulation in China may also remotely connected with other internal climate variability modes, such as the variability over the Pacific, Atlantic, and Arctic ocean (Shabbar *et al.*, 2001; Wu and Wang, 2002; Huang *et al.*, 2006; Park *et al.*, 2010; Cheung *et al.*, 2012; Jiang *et al.*, 2014; Kim *et al.*, 2014; Guan *et al.*, 2015; Xie *et al.*, 2015). For China, the PDO and ENSO were suggested to influence the EAWM especially for the interdecadal variability, and these influences were also modulated by the Arctic Oscillation (Zhou *et al.*, 2007; Wang *et al.*, 2008; Chen *et al.*, 2013; Ding *et al.*, 2014). In addition, as suggested by He *et al.* (2014), the land–sea thermal contrast significantly influenced the atmospheric circulations and blocking. Mori *et al.* (2014) suggested that Arctic sea ice also influenced Eurasian atmospheric circulations and blocking. Thus, the explicit influences from PDO, ENSO, or Arctic on China and the corresponding dynamical mechanisms should be explored in future studies.

Furthermore, the external forcing associated with the reductions in the anthropogenic emissions also were suggested to contribute to the recent global warming hiatus (Estrada *et al.*, 2013). In China, the surface solar radiation experienced the transition from solar dimming to levelling-off circa 1990 (Wang and Dickinson, 2013; Wang and Yang, 2014; Folini and Wild, 2015; Lin *et al.*, 2015), which suggested that the direct solar radiation changes were probably contributed little to the recent warming hiatus in China. The SST-forced reduction of cloud cover was suggested to contribute most to the ceasing of solar dimming around 2000 (Folini and Wild, 2015). However, there are some connections between the aerosols and the atmospheric circulations (Li *et al.*, 2011; Lin *et al.*, 2015; Zhang *et al.*, 2016), and the aerosols also can influence the regional SST, such as over the North Pacific (Yeh *et al.*, 2013). The aerosols were also suggested to have
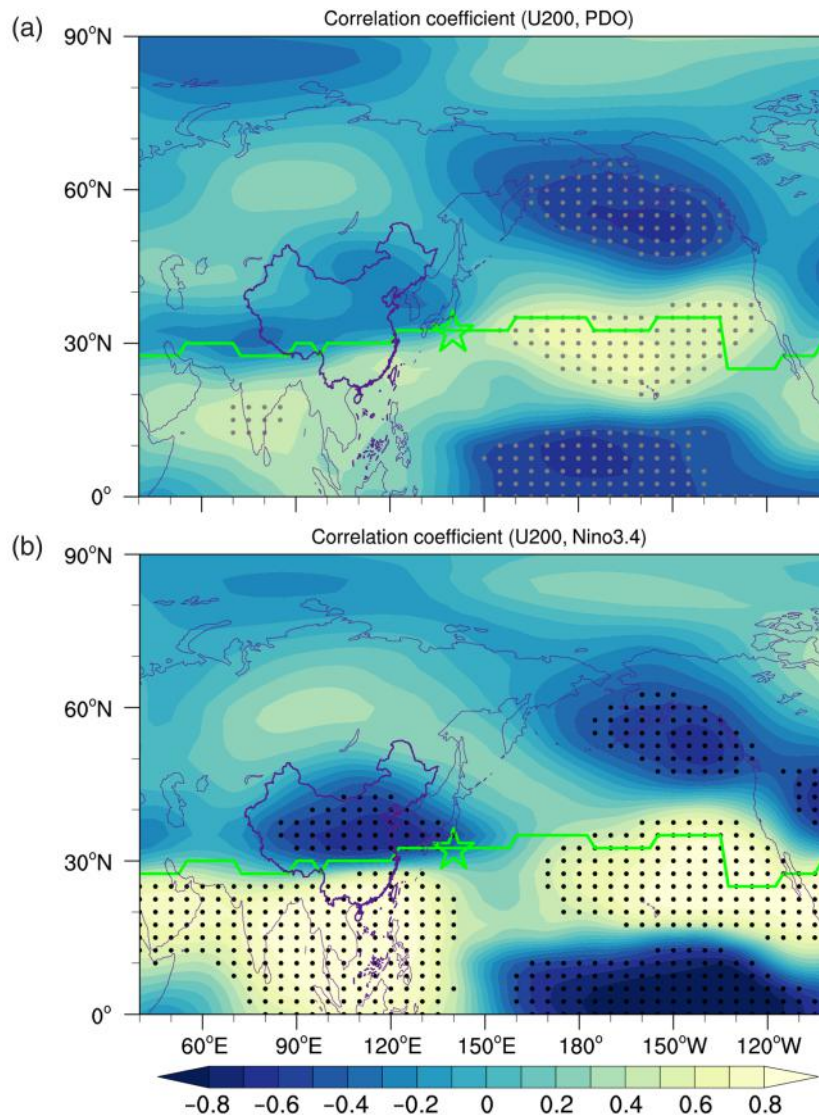
Figure 13. (a) Correlation coefficients between PDO index and 200-hPa zonal winds (U200) during the winter (December to the following February) for the period 1980–2013. The results are the mean of the ERA-interim and NCEP II datasets. The dots represent both the correlation coefficients from ERA-interim and NCEP II were significant at 99% confidence level. The correlation coefficient was calculated using the (Pearson) sample linear cross-correlation method. The corresponding significance was estimated by using the two-tailed Student's *t*-test. The solid curve represents the location with maximum westerly wind speed at each longitude for climatology of 1981–2010, and the pentagram represents the location with maximum westerly wind speed. Note that the climatology of 200-hPa zonal winds was presented in Figure S5. (b) Same as (a) but for correlation coefficients between ENSO index and 200-hPa zonal winds. [Colour figure can be viewed at wileyonlinelibrary.com].

large influences on temperature in China for the regional scales (Su *et al.*, 2008; Liu *et al.*, 2013; Bi *et al.*, 2014; Huang *et al.*, 2014; Liu *et al.*, 2014, 2015; Huang *et al.*, 2016b). In addition, the cloud-radiation feedback was suggested to have induced enhanced warming over the Tibetan Plateau during the recent warming hiatus (Duan and Xiao, 2015). Therefore, the radiative forcing associated with the aerosols and cloud, and their possible influences on the atmospheric circulations in China should also be examined in future studies.

Acknowledgements

Supporting information

The following supporting information is available as part of the online article:
Figure S1. Same as Figure 2 but for using M–K method.
Figure S2. Same as Figure 4 but for using M–K method.
Figure S3. Same as Figure 5 but for using M–K method.
Figure S4. Same as Figure 8 but for using M–K method.

Figure S5. Climatology of the 200-hPa zonal winds during the winter (December to the following February) for the period 1981–2010. Note that the results are the mean of the ERA-interim and NCEP II data sets.

References

Bi J, Shi J, Xie Y, Liu Y, Takamura T, Khatri P. 2014. Dust aerosol characteristics and shortwave radiative impact at a Gobi Desert of northwest China during the spring of 2012. *J. Meteorol. Soc. Jpn.* **92A**: 33–56.

Chen X, Tung K-K. 2014. Varying planetary heat sink led to global-warming slowdown and acceleration. *Science* **345**: 897–903.

Chen W, Lan X, Wang L, Ma Y. 2013. The combined effects of the ENSO and the Arctic Oscillation on the winter climate anomalies in East Asia. *Chin. Sci. Bull.* **58**: 1355–1362.

Cheung HN, Zhou W, Mok HY, Wu MC. 2012. Relationship between Ural-Siberian blocking and the East Asian winter monsoon in relation to the Arctic Oscillation and the El Niño-Southern Oscillation. *J. Clim.* **25**: 4242–4257.

Cohen J, Screen JA, Furtado JC, Barlow M, Whittleston D, Coumou D, Francis J, Dethloff K, Entekhabi D, Overland J, Jones J. 2014. Recent Arctic amplification and extreme mid-latitude weather. *Nat. Geosci.* **7**: 627–637.

D'Andrea F, Tibaldi S, Blackburn M, Boer G, Déqué M, Dix MR, Dugas B, Ferranti L, Iwasaki T, Kitoh A, Pope V. 1998. Northern Hemisphere atmospheric blocking as simulated by 15 atmospheric general circulation models in the period 1979–1988. *Clim. Dyn.* **14**: 385–407.

Dai A, Fyfe JC, Xie SP, Dai X. 2015. Decadal modulation of global surface temperature by internal climate variability. *Nat. Clim. Change* **5**: 555–559.

Dee DP, Uppala SM, Simmons AJ, Berrisford P, Poli P, Kobayashi S, Andrae U, Balmaseda MA, Balsamo G, Bauer P, Bechtold P. 2011. The ERA-interim reanalysis: configuration and performance of the data assimilation system. *Q. J. R. Meteorol. Soc.* **137**: 553–597.

Ding Y, Liu Y, Liang S, Ma X, Zhang Y, Si D, Liang P, Song Y, Zhang J. 2014. Interdecadal variability of the East Asian winter monsoon and its possible links to global climate change. *J. Meteorol. Res.* **28**: 693–713.

Duan A, Xiao Z. 2015. Does the climate warming hiatus exist over the Tibetan Plateau? *Sci. Rep.* **5**: 13711, doi: 10.1038/srep13711.

England MH, McGregor S, Spence P, Meehl GA, Timmermann A, Cai W, Gupta AS, McPhaden MJ, Purich A, Santoso A. 2014. Recent intensification of wind-driven circulation in the Pacific and the ongoing warming hiatus. *Nat. Clim. Change* **4**: 222–227.

England MH, Kajtar JB, Maher N. 2015. Robust warming projections despite the recent hiatus. *Nat. Clim. Change* **5**: 394–396.

Estrada F, Perron P, Martínez-López B. 2013. Statistically derived contributions of diverse human influences to twentieth-century temperature changes. *Nat. Geosci.* **6**: 1050–1055.

Folini D, Wild M. 2015. The effect of aerosols and sea surface temperature on China's climate in the late twentieth century from ensembles of global climate simulations. *J. Geophys. Res. Atmos.* **120**: 2261–2279.

Fyfe JC, Meehl GA, England MH, Mann ME, Santer BD, Flato GM, Hawkins E, Gillett NP, Xie SP, Kosaka Y, Swart NC. 2016. Making sense of the early-2000s warming slowdown. *Nat. Clim. Change* **6**: 224–228.

Gong DY, Wang SW, Zhu JH. 2001. East Asian winter monsoon and Arctic Oscillation. *Geophys. Res. Lett.* **28**: 2073–2076.

Guan X, Huang J, Guo R, Lin P. 2015. The role of dynamically induced variability in the recent warming trend slowdown over the Northern Hemisphere. *Sci. Rep.* **5**: 12669, doi: 12610.11038/srep12669.

Harris IP, Jones PD, Osborn TJ, Lister DH. 2014. Updated high-resolution grids of monthly climatic observations – the CRU TS3.10 Dataset. *Int. J. Climatol.* **34**: 623–642.

He Y, Huang J, Ji M. 2014. Impact of land–sea thermal contrast on interdecadal variation in circulation and blocking. *Clim. Dyn.* **43**: 3267–3279.

Hersbach H, Peubey C, Simmons A, Berrisford P, Poli P, Dee D. 2015. ERA-20CM: a twentieth-century atmospheric model ensemble. *Q. J. R. Meteorol. Soc.* **141**: 2350–2375.

Higuchi K, Huang J, Shabbar A. 1999. A wavelet characterization of the North Atlantic Oscillation variation and its relationship to the North Atlantic sea surface temperature. *Int. J. Climatol.* **19**: 1119–1129.

Huang J, Higuchi K, Shabbar A. 1998. The relationship between the North Atlantic Oscillation and El Niño-Southern Oscillation. *Geophys. Res. Lett.* **25**: 2707–2710.

Huang J, Ji M, Higuchi K, Shabbar A. 2006. Temporal structures of the North Atlantic Oscillation and its impact on the regional climate variability. *Adv. Atmos. Sci.* **23**: 23–32.

Huang J, Guan XD, Ji F. 2012. Enhanced cold-season warming in semi-arid regions. *Atmos. Chem. Phys.* **12**: 5391–5398.

Huang J, Wang T, Wang W, Li Z, Yan H. 2014. Climate effects of dust aerosols over East Asian arid and semiarid regions. *J. Geophys. Res. Atmos.* **119**: 11398–11416.

Huang J, Ji M, Xie Y, Wang S, He Y, Ran J. 2016a. Global semi-arid climate change over last 60 years. *Clim. Dyn.* **46**: 1131–1150.

Huang J, Yu H, Guan X, Wang G, Guo R. 2016b. Accelerated dryland expansion under climate change. *Nat. Clim. Change* **6**: 166–171.

IPCC. 2013. Climate change 2013: the physical science basis. In *Contribution of Working Group I to the Fifth Assessment Report of the Intergovernmental Panel on Climate Change*, Stocker TF, Qin D, Plattner GK, Tignor M, Allen SK, Boschung J, Nauels A, Xia Y, Bex V, Midgley PM. (eds). Cambridge University Press: Cambridge, UK and New York, NY.

Ji F, Wu Z, Huang J, Chassignet EP. 2014. Evolution of land surface air temperature trend. *Nat. Clim. Change* **4**: 462–466.

Jiang Z, Yang H, Liu Z, Wu Y, Wen N. 2014. Assessing the influence of regional SST modes on the winter temperature in China: the effect of tropical Pacific and Atlantic. *J. Clim.* **27**: 868–879.

Kanamitsu M, Ebisuzaki W, Woollen J, Yang SK, Hnilo JJ, Fiorino M, Potter GL. 2002. NCEP-DOE AMIP-II reanalysis (R-2). *Bull. Am. Meteorol. Soc.* **83**: 1631–1643.

Karl TR, Arguez A, Huang B, Lawrimore JH, McMahon JR, Menne MJ, Peterson TC, Vose RS, Zhang HM. 2015. Possible artifacts of data biases in the recent global surface warming hiatus. *Science* **348**: 1469–1472.

Kendall MG. 1948. *Rank Correlation Methods*, 5th edn. E. Arnold: London, 320 pp.

Kim JW, Yeh SW, Chang EC. 2014. Combined effect of El Niño-Southern oscillation and Pacific Decadal Oscillation on the East Asian winter monsoon. *Clim. Dyn.* **42**: 957–971.

Kosaka Y, Xie S-P. 2013. Recent global-warming hiatus tied to equatorial Pacific surface cooling. *Nature* **501**: 403–407.

Lee J, Lund R. 2004. Revisiting simple linear regression with autocorrelated errors. *Biometrika* **91**: 240–245.

Lewandowsky S, Risbey JS, Oreskes N. 2015. The "pause" in global warming: turning a routine fluctuation into a problem for science. *Bull. Am. Meteorol. Soc.* 723–733, doi: 10.1175/BAMS-D-14-00106.1.

Li Q, Zhang H, Chen JI, Li W, Liu X, Jones P. 2009. A mainland China homogenized historical temperature dataset of 1951–2004. *Bull. Am. Meteorol. Soc.* **90**(8): 1062–1065.

Li D, Wang J, Li Z, Liu H. 2011. Snow/rainfall anomaly in winter of northern China and associated atmospheric circulation and aerosol distribution features. *Acta Meteorol. Sin.* **25**: 783–796.

Li J, Sun C, Jin FF. 2013. NAO implicated as a predictor of Northern Hemisphere mean temperature multidecadal variability. *Geophys. Res. Lett.* **40**: 5497–5502.

Li Q, Yang S, Xu W, Wang XL, Jones P, Parker D, Zhou L, Feng Y, Gao Y. 2015. China experiencing the recent warming hiatus. *Geophys. Res. Lett.* **42**: 889–898.

Lin C, Yang K, Huang J, Tang W, Qin J, Niu X, Chen Y, Chen D, Lu N, Fu R. 2015. Impacts of wind stilling on solar radiation variability in China. *Sci. Rep.* **5**: 15135, doi: 10.1038/srep15135.

Liu Y, Shi G, Xie Y. 2013. Impact of dust aerosol on glacial-interglacial climate. *Adv. Atmos. Sci.* **30**: 1725–1731.

Liu Y, Jia R, Dai T, Xie Y, Shi G. 2014. A review of aerosol optical properties and radiative effects. *J. Meteorol. Res.* **28**: 1003–1028.

Liu Y, Sato Y, Jia R, Xie Y, Huang J, Nakajima T. 2015. Modeling study on the transport of summer dust and anthropogenic aerosols over the Tibetan Plateau. *Atmos. Chem. Phys.* **15**: 12581–12594.

Mann HB. 1945. Nonparametric tests against trend. *Econometrica* **13**: 245–259.

Meehl GA, Teng H, Arblaster JM. 2014. Climate model simulations of the observed early-2000s hiatus of global warming. *Nat. Clim. Change* **4**: 898–902.

Mori M, Watanabe M, Shiogama H, Inoue J, Kimoto M. 2014. Robust Arctic sea-ice influence on the frequent Eurasian cold winters in past decades. *Nat. Geosci.* **7**: 869–873.

Park TW, Ho CH, Yang S. 2010. Relationship between the Arctic Oscillation and cold surges over East Asia. *J. Clim.* **24**: 68–83.

Roberts CD, Palmer MD, McNeall D, Collins M. 2015. Quantifying the likelihood of a continued hiatus in global warming. *Nat. Clim. Change* **5**: 337–342, doi: 10.1038/nclimate2531.

Screen JA, Simmonds I. 2014. Amplified mid-latitude planetary waves favour particular regional weather extremes. *Nat. Clim. Change* **4**: 704–709.

Shabbar A, Huang J, Higuchi K. 2001. The relationship between the wintertime North Atlantic Oscillation and blocking episodes in the North Atlantic. *Int. J. Climatol.* **21**: 355–369.

Steinman BA, Mann ME, Miller SK. 2015. Atlantic and Pacific multi-decadal oscillations and Northern Hemisphere temperatures. *Science* **347**: 988–991.

Su J, Huang J, Fu Q, Minnis P, Ge J, Bi J. 2008. Estimation of Asian dust aerosol effect on cloud radiation forcing using Fu-Liou radiative model and CERES measurements. *Atmos. Chem. Phys.* **8**: 2763–2771.

Trenberth KE. 2015. Has there been a hiatus? *Science* **349**: 691–692.

Trenberth KE, Fasullo JT, Branstator G, Phillips AS. 2014. Seasonal aspects of the recent pause in surface warming. *Nat. Clim. Change* **4**: 911–916.

Wallace JM, Fu Q, Smoliak BV, Lin P, Johanson CM. 2012. Simulated versus observed patterns of warming over the extratropical Northern Hemisphere continents during the cold season. *Proc. Natl. Acad. Sci.* **109**: 14337–14342.

Wang L, Chen W. 2014. An intensity index for the East Asian winter monsoon. *J. Clim.* **27**: 2361–2374.

Wang K, Dickinson RE. 2013. Contribution of solar radiation to decadal temperature variability over land. *Proc. Natl. Acad. Sci.* **110**: 14877–14882.

Wang XL, Swail VR. 2001. Changes of extreme wave heights in Northern Hemisphere oceans and related atmospheric circulation regimes. *J. Clim.* **14**: 2204–2221.

Wang YW, Yang YH. 2014. China's dimming and brightening: evidence, causes and hydrological implications. *Ann. Geophys.* **32**: 41–55.

Wang L, Chen W, Huang R. 2008. Interdecadal modulation of PDO on the impact of ENSO on the East Asian winter monsoon. *Geophys. Res. Lett.* **35**: L20702, doi: 10.1029/2008GL035287.

Wang YH, Yeh CH, Young HW, Hu K, Lo MT. 2014. On the computational complexity of the empirical mode decomposition algorithm. *Physica A* **400**: 159–167.

Wu B, Wang J. 2002. Winter Arctic Oscillation, Siberian high and East Asian winter monsoon. *Geophys. Res. Lett.* **29**: 1897, doi: 10.1029/2002GL015373.

Xie Y, Liu Y, Huang J. 2015. Overestimated Arctic warming and underestimated Eurasia mid-latitude warming in CMIP5 simulations. *Int. J. Climatol.*, doi: 10.1002/joc.4644.

Xu W, Li Q, Wang XL, Yang S, Cao L, Feng Y. 2013. Homogenization of Chinese daily surface air temperatures and analysis of trends in the extreme temperature indices. *J. Geophys. Res. Atmos.* **118**: 9708–9720.

Yeh SW, Kim WM, Kim YH, Moon BK, Park RJ, Song CK. 2013. Changes in the variability of the North Pacific sea surface temperature caused by direct sulfate aerosol forcing in China in a coupled general circulation model. *J. Geophys. Res. Atmos.* **118**: 1261–1270.

Zhang Y, Ding A, Mao H, Nie W, Zhou D, Liu L, Huang X, Fu C. 2016. Impact of synoptic weather patterns and inter-decadal climate variability on air quality in the North China Plain during 1980–2013. *Atmos. Environ.* **124**: 119–128.

Zhou W, Wang X, Zhou TJ, Li C, Chan JC. 2007. Interdecadal variability of the relationship between the East Asian winter monsoon and ENSO. *Meteorol. Atmos. Phys.* **98**: 283–293.